The Electro-Oxidation of H_2, CO in a Model PEM Fuel Cell: Oscillations, Chaos, Pulses

Sebastian Kirsch,[a] Richard Hanke-Rauschenbach,[a,*,z] Bianka Stein,[a] Ralf Kraume,[b,*] and Kai Sundmacher[a,c]

[a]*Max Planck Institute for Dynamics of Complex Technical Systems, 39106 Magdeburg, Germany*
[b]*S++ Simulation Service, 82418 Murnau-Westried, Germany*
[c]*Process Systems Engineering, Otto-von-Guericke University Magdeburg, 39106 Magdeburg, Germany*

H_2, CO electro-oxidation in a model PEM Fuel Cell (PEMFC) is investigated at 37°C with the help of distributed current measurements. The main purpose of the experiments is to verify the formation of spatio-temporal patterns that have been predicted for a PEMFC with straight channels and a H_2 evolving cathode. For galvanostatic operation and a high feed flow rate well expressed globally coupled oscillations are found. For decreasing feed flow rate a period doubling bifurcation cascade appears. Potentiostatic control provokes the breakage of the strict phase relation between adjacent oscillators and the appearance of pulses as well as turbulence is seen. The turbulence is enhanced if an oxygen reducing cathode is introduced instead of a hydrogen evolving cathode. All the findings are compared to existing predictions. The study of the patterns is of interest for PEMFC engineers as they directly determine the CO tolerance behavior of the PEMFC.
© 2013 The Electrochemical Society. [DOI: 10.1149/2.002306jes] All rights reserved.

Introduction

Polymer electrolyte membrane fuel cells (PEMFCs) are considered to be promising and very efficient energy converters which convert hydrogen with the oxygen contained in the ambient air into electrical energy. When H_2 is generated from hydrocarbon sources it might contain small amounts of carbon monoxide, CO (e.g. in case of stationary H_2 generation from autothermal reforming, steam or dry reforming). Unfortunately, CO adsorbs on the Pt catalyst surface and passivates it. Even traces of less than 20 ppm can easily lead to voltage losses of more than 500 mV,[1] where otherwise the H_2 oxidation in absence of CO does not consume more than 30 mV in total.[2] The application of $PtRu$ anode catalysts reduces these 500 mV (found for Pt) to below 350 mV.[3]

In 2002 Zhang and Datta investigated the H_2, CO electro-oxidation on a $PtRu$ anode under galvanostatic control and found that the cell voltage oscillates with an amplitude of about 350 mV once a certain critical current was exceeded.[4] They noticed that, due to the non-sinusoidal shape of the oscillations, the cell voltage loss in the temporal mean was far lower compared to potentiostatic control, where no oscillations were seen.[5] In a different work[6] it was shown that the oscillations can be understood as an autonomous self-cleaning process of the anode in which CO is periodically oxidized. Oscillations of the cell voltage under galvanostatic control were later also found for Pt[1] and $PtPd$[7] catalysts. In fact, with the help of the oscillations it seems possible to reduce the additional anodic losses to 200 mV in the case of pure Pt and to 100 mV in the case of $PtRu$.[8] However, an additional reduction of anodic losses is necessary in order to create sufficiently CO-tolerant PEMFC anodes for commercialization.

A mathematical model for H_2, CO electro-oxidation in a homogeneous PEMFC with a $PtRu$ anode that qualitatively describes the measured oscillations stems from Ref. 4. Recently, the model was rigorously extended into an along-the-channel model which also allows spatial variations along the direction of the gas flow.[9] Later, this model was simplified in order to increase its transparency.[10] It was found that the spatially extended model can be understood as a series of locally acting oscillators with a parameter gradient- and two different kinds of interactions between them.

On the one hand, a global coupling term, introduced by the galvanostatic constraint, leads to a distance independent interaction of the individual oscillators. On the other hand, migration coupling, indicating lateral currents in the membrane, leads to a local interaction of adjacent oscillators. The variation of the different terms caused in the simulation a couple of scenarios that are supposed to influence the

CO tolerance of the PEMFC.[11] The objective of this manuscript is to validate the predicted patterns.

The paper is organized as follows: Initially, a measurement device that is capable of fast scans of the locally distributed current distribution and other experimental details are explained. In the following section, the mechanistic details of galvanostatic H_2, CO electro-oxidation are introduced and the predictions raised in Refs. 9 and 10 are summarized. In section four, experiments on galvanostatic H_2, CO electro-oxidation are presented and for the first time spatially resolved. Subsequently, the theory developed so far only for galvanostatic control is generalized for the case of potentiostatic control and related experiments are presented. Finally, the influence of the counter electrode is experimentally investigated and theoretically rationalized.

Experimental: Setup and Design

Initially in this section, the fuel cell setup for distributed current density measurement is introduced. Next, the preparation of the membrane electrode assembly is described. Afterwards the test stand is sketched and the conditioning procedure is depicted. Finally, the setup and the applied parameters for the following experiments are given.

Measurement device.— The measurement of the current distribution in a PEMFC has been proven to be a very helpful tool to investigate spatial inhomogeneities.[12] With its help, flow field design and operation conditions have been successively optimized in recent years (e.g. 13). Several methods to measure the current distribution are reported in the literature. The three most important techniques are either based on the application of (1) a printed circuit board (PCB),[14,15] (2) a resistor network,[16,17] or (3) an array of Hall effect sensors.[18,19] The PCB technique was introduced in 1998 by Cleghorn et al.[14] and is based on the replacement of one current collector by a PCB. The PCB is segmented, whereby each segment has an individual electrically isolated pathway for current collection. The big advantages of the PCB technology compared to the other techniques are its simple implementation and its high spatial and temporal resolution.

For the present study, a device for the measurement of the current distribution, based on PCB technology, has been developed by S++ Simulation Services (Fig. 1a–1b). The device is shown in Fig. 1c. It is based on the measurement of voltages across multiple shunt resistors which are integrated into the PCB (trade name: Current Scan Shunt). The resistance of an individual shunt resistor is ≈7 mΩ.

The device is constructed as follows: Initially, the shunt resistors are prepared by etching a special foil with a very low temperature coefficient. Then, the foil is embedded into a printed circuit board referred to as sensor plate. Afterwards, the shunt resistors are connected with

*Electrochemical Society Active Member.
zE-mail: hanke-rauschenbach@mpi-magdeburg.mpg.de
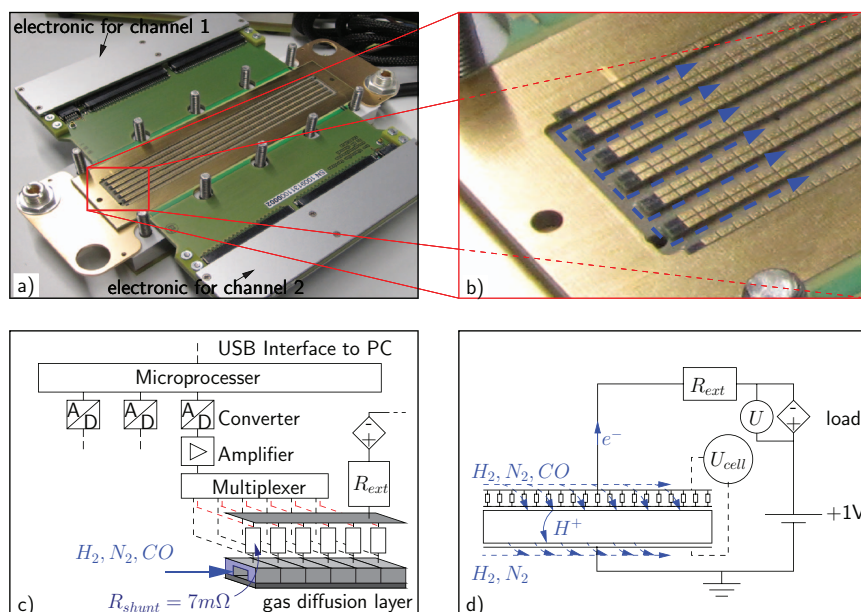
Figure 1. a) The segmented anode flow field with 80 segments per channel (channel length: 14.4 cm). The both inner channels are used for current distribution measurement, while the outer channels serve for homogenization. b) Each segment consists of two sub-segments that face across the channel. c) The scheme depicts how the current is read with the help of small shunt resistors. d) The setup shows how the cell was implemented into the test stand. R_{ext} stands for the line resistances.

vias to the contact segments on the top and the bottom of the sensor plate. A multiplexer, responsible for read out 8 shunts successively, is connected to the segments. The multiplexer signal is amplified and passed into an analog digital converter. Finally, the signal is sent to the PC via USB interface. After calibration the actual current density profile is obtained.

In Fig. 1 a-b the sensor plate is shown. Six parallel gas channels are machined into it. They are 14.4 cm in length and 4 mm in width (2 mm land and 2 mm channel). Each channel is equipped with 80 contact segments (and 10 multiplexers). Each segment is divided into two sub-segments left and right of the channel (Fig. 1b). The sub-segments were first galvanically plated with gold and then covered with a highly conductive anti-corrosive carbon varnish (not shown). The active area of a segment is 1.8·4 mm^2. Only the two inner channels are connected to read-out electronics (Fig. 1a), the other channels are equipped with shunt resistors due to symmetry reasons. The minimum sampling time for a complete scan is 15 ms. The data is stored in ASCII format and analyzed with MATLAB for presentation.

Fuel cell preparation and conditioning.— After initial activation of a Nafion membrane in hydrogen peroxide (5% in H_2O), subsequent boiling in sulphuric acid (1 M), and final storage in Millipore water, the membrane (for thickness see Tab. I) was spray-coated with the catalyst ink. The cathode catalyst ink was composed of Pt, purchased from Alfa Aesar, and 10 $wt\%$ Nafion (related to dry catalyst) dissolved in sufficient Millipore water. The anode catalyst contained $PtRu$ 50/50

instead of pure Pt but was identical in the other respects. The anode catalyst loading was chosen to be 2 mg cm^{-2} and 1 mg cm^{-2} for the cathode. The spray painted area was (144 · 22) mm^2 in size.

The fuel cell was then assembled with the prepared MEA and 200 μm-thick Toray papers that were surrounded by 170 μm PTFA-sealing. The cell was then connected to a FuelCon test stand which allows for convenient automatic control of the cell conditions via a predefined user interface. In short, each of the two gas lines contained several mass flow controllers for different gases (plus additional valves for the full shut down of the inlets) followed by bubbler bottles, heating hoses between the bubblers and the cell (temperature always 5 K higher than cell temperature), a water collector in the cathode line and backpressure valves.

During conditioning, the cell was fed with 1000 mL min^{-1} hydrogen and 1500 mL min^{-1} air and held at 60°C cell temperature ($rH = 100\%$). Then, the cell voltage was set to 0.85 V for 15 mins before it was held at 0.60 V for 10 mins and finally at open circuit voltage (ocv) for 3 mins. This cycle was carried out five times. Afterwards, the gas lines were flipped and the cycle was carried out five times again.

Experimental procedure.— For the following experiments, the two inlets of the anode side were set up with H_2 (purity: 5.0) and a mixture of N_2 and 1% CO (purity: 4.8 for the N_2). Usually, the feed flow rates were 180- and 20 mLmin^{-1}, respectively. On the cathode side, a H_2, N_2 mixture was used for most of the experiments. The H_2 to

Table I. Operating conditions for the following experiments. T_{dp} and p stand for the dew point temperature and the backpressure in both gas lines, $F_{H2,in}^{a,\theta}$ and $F_{(N2,CO),in}^{a,\theta}$ represent the feed flow rate of H_2 and the N_2, CO mixture at the inlet at standard conditions. Oppositely, the differently indexed $F_{i,in}^{c,\theta}$ represent the type of feed gas ($i \in [(N2, CO), N2, air]$) and its feed flow rate into the cathode. d_m is the membrane thickness.

Fig.	T_{cell} [°C]	T_{dp} [°C]	p [bar]	$F_{H2,in}^{a,\theta}$, $F_{(N2,CO),in}^{a,\theta}$ [mL min^{-1}]	$F_{N2,in}^{c,\theta}$, $F_{N2,in}^{c,\theta}$ [mL min^{-1}]	d_m [μm]
2	37	32	1.1	40, 40	20, 180	89
3	37	32	1.1	180, 20	20, 180	89
4	37	32	1.1	variable	20, 180	89
5	37	32	1.1	126, 14	20, 180	89
6	variable	variable	1.1	180, 20	20, 180	89
7–8	37	32	1.1	180, 20	20, 180	89

Fig.	T_{cell} [°C]	T_{dp} [°C]	p [bar]	$F_{H2,in}^{a,\theta}$, $F_{(N2,CO),in}^{a,\theta}$ [mL min^{-1}]	$F_{air,in}^{c,\theta}$ [mL min^{-1}]	d_m [μm]
9–10	37	32	1.1	180, 20	1000	179

N_2 ratio was chosen to be 10 % in order to minimize H_2 diffusion toward the anode but still to guarantee a well defined electrode. In addition, two experiments were also carried out with an air-fed cathode. To avoid any uncertainty the important operational parameters for all experiments are collected in Tab. I. Please note, that a thicker membrane was applied in the case of the air-fed cathode. The reason for this choice will become clear in the discussion. Throughout all the experiments the cell was operated in co-flow arrangement.

As the electric load of the test stand (Höcherl and Hackl ZS Electronic Load) can only work passively, an additional voltage supply device (Statron Power Supply 2257.8, maximum voltage: 4.0 V, maximum current: 100 A) was used if the H_2-fed cathode was used (Fig. 1d). Its negative pole was attached to the cathode while the positive pole was connected to the load. The source was operated in current limiting mode with a set-up voltage of 1.000 V. In initial tests it was ensured that the voltage is stable for varying currents up to 30 A (maximal deviation <10 mV). For operation with an air-fed cathode, the source was removed from the circuit.

The load allowed for galvanostatic- as well as for potentiostatic control. The total resistance of all lines was measured to be $7 \pm 1\,\text{m}\Omega$. For impedance measurements at 1 kHz a RCL meter (Fluke PM6303A Automatic RCL Meter) was used while the system was at ocv.

Mechanistic Details and Predictions at Galvanostatic Control

The aim of this paper is the experimental investigation of pattern formation during H_2, CO electro-oxidation in a PEMFC with straight channel geometry. Specific patterns for galvanostatic operation were predicted recently in two theoretical works.[9,10]

The purpose of this section is to establish a simple theoretical framework from which the different patterns can be anticipated. The framework allows the reader to understand the patterns as a result of local dynamics and interactions between reaction sites. Initially, the model equations of the homogeneous system (where the interactions are negligible) are introduced. Then, the model equations of the inhomogeneous system are depicted. The occurrence of the different patterns is rationalized from the comparison of both models.

Homogeneous system.— Cell voltage oscillations during the galvanostatic H_2, CO electro-oxidation in a PEMFC were first investigated in Ref. 4. Due to the design of the experiments in 4 (high feed flow rates, galvanostatic control) the system can be considered to be homogeneous. Homogeneous systems can be modeled with the help of ordinary differential equations (ODEs). An ODE model, which reproduced the oscillations was also published in Ref. 4. With the help of this model it was found that water dissociation, which leads to voltage dependent surface passivation by OH, is the main reason for the oscillations.[20] In addition, the system was characterized as an HN-NDR oscillator, following the classification scheme for nonlinear electrochemical systems introduced by Krischer.[21] However, the details of the phenomenon are not important here. A detailed analysis of the homogeneous system can be found in Ref. 22.

Instead, it is more relevant for the present work that the ODE model developed in 4 was shown to be reducible. The reduced model shows all the phenomena of the original formulation (including the oscillations) and is derived in Ref. 22. While the initial formulation comprises five ODEs, the reduced model contains only two ODEs. Thus, the two ODEs may be seen as describing a simple oscillator (like the Van der Pol oscillator or the Lotka-Volterra model) after the onset of oscillations. They describe the evolution of the anodic double layer voltage $\Delta\varphi_a$ and the CO surface coverage θ_{CO}

$$c_{dl}\frac{d\Delta\varphi_a}{dt} = \frac{I_{load}}{A} - f(\Delta\varphi_a, \theta_{CO}), \qquad [1]$$

$$\gamma C_t^* \frac{d\theta_{CO}}{dt} = g(\Delta\varphi_a, \theta_{CO}, x_{CO,in}, F_{in}). \qquad [2]$$

The function $f(\Delta\varphi_a, \theta_{CO})$ represents the faradaic reaction current and $g(\Delta\varphi_a, \theta_{CO}, x_{CO,in}, F_{in})$ represents the sum of CO adsorption-

and CO oxidation rates. Again, their specific formulation is not important here. The parameters in Eqs. (1)–(2) are the electric double layer capacity c_{dl}, the material double layer capacity γC_t^*, the current density applied by the load per geometric surface area I_{load}/A, the molar feed flow rate F_{in} and the molar CO fraction at the inlet $x_{CO,in}$. The last two parameters are of major importance as they are easily found experimentally and primarily determine the details of the oscillation (frequency, amplitude, etc.).

Inhomogeneous system.— The model for the inhomogeneous system, describing H_2, CO electro-oxidation in a PEMFC with straight channel geometry, was derived in Ref. 9 and simplified in Ref. 10. It was concluded that the two following partial differential equations (PDEs) dominate the dynamic behavior

$$c_{dl}\frac{\partial\Delta\varphi_a}{\partial t} = \frac{I_{load}}{A} - f(\Delta\varphi_a, \theta_{CO}) + \frac{d_m^2}{3AR_\Omega L^2}\frac{\partial^2\Delta\varphi_a}{\partial\zeta^2}$$
$$+ \frac{1}{AR_\Omega}(\overline{\Delta\varphi_a} - \Delta\varphi_a), \qquad [3]$$

$$\gamma C_t^* \frac{\partial\theta_{CO}}{\partial t} = g(\Delta\varphi_a, \theta_{CO}, x_{CO}), \qquad [4]$$

with $\overline{\Delta\varphi_a}$ standing for the spatial average

$$\overline{\Delta\varphi_a} = \int_0^1 \Delta\varphi_a d\zeta. \qquad [5]$$

Equations (3)–(4) describe the evolution of the anodic double layer voltage $\Delta\varphi_a$ and the CO surface coverage θ_{CO} as a function of time t and channel coordinate ζ ($\zeta \in [0\,(\text{inlet}), 1\,(\text{outlet})]$). The boundary conditions for Eq. (3) are

$$\frac{\partial\Delta\varphi_a}{\partial\zeta}\Big|_{\zeta=0} = \frac{\partial\Delta\varphi_a}{\partial\zeta}\Big|_{\zeta=1} = 0. \qquad [6]$$

However, the dynamics of the CO transport along the channel might influence the overall behavior at specific conditions,[9] such that the local molar CO fraction in the channel x_{CO} need in general to be described by

$$\frac{\partial x_{CO}}{\partial t} = -\frac{1}{V}\frac{\partial}{\partial\zeta}(x_{CO}F(\Delta\varphi_a, \theta_{CO}, x_{CO}))$$
$$- \frac{RT}{p}\frac{1}{h}r_{CO,ad}(\Delta\varphi_a, \theta_{CO}, x_{CO}), \qquad [7]$$

with the boundary conditions

$$x_{CO}(\zeta = 0, t) = x_{CO,in}(t). \qquad [8]$$

The function $r_{CO,ad}(\Delta\varphi_a, \theta_{CO}, x_{CO})$ mimics the rate of CO adsorption while $F(\Delta\varphi_a, \theta_{CO}, x_{CO})$ represents the local molar feed flow rate. The explicit formulation of these two functions can be found in 10. New parameters are the membrane resistance R_Ω, the volume- and the length of the channel V and L, the thickness of the membrane d_m and the height of the channel h. The other parameters R, p, T represent the gas constant, the cell pressure and the cell temperature, respectively.

The equations can be understood in a simple manner. First of all, apart from the two right terms in Eq. (3), the first two equations Eqs. (3)–(4) reflect the homogeneous system (Eq. (1)–(2)), indicating that the channel can be understood as a series of individual oscillators. Second, due to the fact that $g(\Delta\varphi_a, \theta_{CO}, x_{CO})$ of the local oscillator depends on the local molar CO fraction x_{CO} and as CO might be oxidized, the conditions for the individual oscillators change along the channel according to Eq. (7). Finally, the two terms on the right end of Eq. (3) represent electric coupling terms between different oscillators. While the first term stands for a local coupling of adjacent oscillators (second order derivative: migration coupling), the right term represents global coupling (mean-field coupling). Dependent on the parameters controlling these terms ($\frac{d_m^2}{3AR_\Omega L^2}$ and $\frac{1}{AR_\Omega}$), the one or the other might be dominant. The following paragraphs give an

overview about the scenarios that are used to predict the influence of the coupling terms.[9,10]

For dominant mean-field coupling and a large excess of gas it is expected that the system behaves like a homogeneous system. This means that all oscillators express a unique frequency and are in phase. The measurement of integral information (cell voltage, cell current) yield the spatially averaged oscillation, found by Zhang et al.[4] According to the simulation, a decrease in the molar feed flow rate F_{in} leads to a period doubling bifurcation of the homogeneous oscillation.[9] This behavior was claimed to be found experimentally by Mota et al.,[23] who found a period doubling bifurcation for decreasing flow rate. However, a detailed comparison with the model prediction is not straight forward for two reasons: One, the model-based predictions in Refs. 9 and 10 were generated in the form of spatio-temporal plots of inner variables (e.g. the current density as a function of channel position and time) but the study of Mota et al. provided only integral information (like an average current density). Two, the geometry for the model was a single one-dimensional channel, but a serpentine geometry in Ref. 23.

In contrast to dominant mean-field coupling, where globally synchronized oscillations are expected, a totally different scenario is suggested by the model for dominant migration coupling, namely the appearance of spatio-temporal turbulence.[10] The turbulence might appear in two flavors. Either the system expresses phase turbulence, evident by small disturbances in the phase relation between adjacent oscillators, or defect turbulence occurs, characterized by phase slips (local aperiodic breakdowns of the oscillation amplitude). Yet, there is no experimental evidence for spatio-temporal turbulence during H_2, CO electro-oxidation in a PEMFC in the literature. In order to find this behavior it was argued in Ref. 10 that the membrane resistance R_Ω might be reasonable parameter for switching from the globally coupled- to the spatio-temporal chaotic scenario.

Experimental Results and Discussion

The discussion will begin with a detailed investigation of galvanostatic control. The control parameters of these experiments are the current density, the feed flow rate, the cell temperature and the dew point temperature. Afterwards, potentiostatic control will be considered with a focus onto the influence of the cell voltage and the cathode.

Galvanostatic H_2, CO oxidation.— In this subsection, the results of galvanostatic H_2, CO electro-oxidation for a single predefined current are presented first to familiarize the reader with the principal information of such a measurement and also to sketch basic behavior. Next, current scans are introduced as a method to quickly search for bifurcation points. Afterwards, qualitatively different behaviors occurring under the influence of varied current and feed flow rate will be considered in detail. Finally, results are presented for varying humidity.

Behavior at constant current.—Fig. 2 shows the spatio-temporal plots of the current density distributions in the two screened channels as well as the time series of the cell voltage and the average current in the observed cell area during galvanostatic control.

In Fig. 2c it can be seen that the cell voltage oscillates within a period of several seconds and has an amplitude of 500 mV typical for *PtRu* catalyst.[8] This time series resembles the information that is obtained with a conventional fuel cell (without spatially distributed current measurement). Assuming a homogeneous system, this time series was successfully modeled[4,7] and is well understood.[22] From the model perspective, the phenomenon can be rationalized as follows:

Whenever the cell voltage has recovered from minimal values (e.g. at $t = 11$ s in Fig. 2) the electro-active surface has minimum CO coverage. From then on, as CO enters the cell with the feed stream, CO adsorbs onto the *PtRu* and hinders the oxidation of H_2. Because the current is set to be constant, the anodic overvoltage (a driving force for H_2 oxidation) needs to increase. This leads to a decrease in the cell voltage. At a specific overvoltage (approx. 350 mV on *PtRu*[24,22])
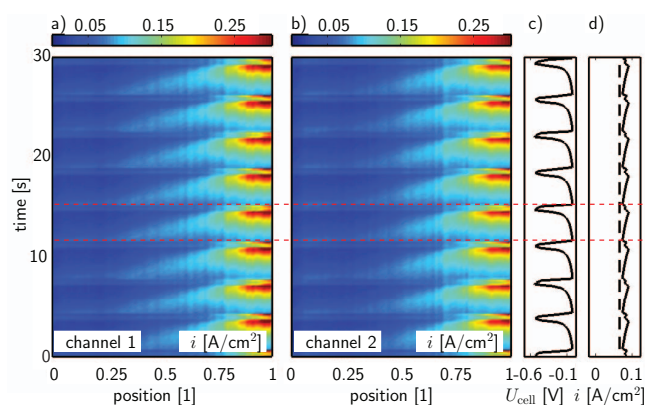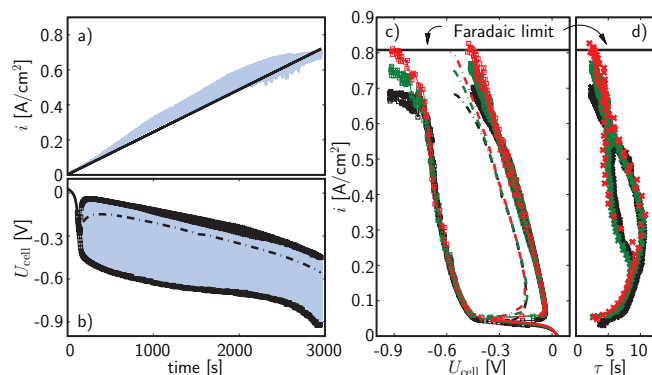

Figure 2. Experimental results for galvanostatic H_2 electro-oxidation in a PEM fuel cell under influence of 5000 ppm *CO* for an integral current of 2 A. a-b) The spatio-temporal evolution of the current density in the two channels under observation. c) The related time series of the cell voltage. d) The related time series of the mean current density, averaged about the both channels (continuous line), as well as the setup current density (dashed line).

dissociation of water begins . This has two different effects. On one hand this process leads to a further reduction in the surface available for H_2 oxidation but on the other hand it also provides the reactant for the oxidation of CO. As long as the overvoltage is increasing further the total coverage (by oxides and CO) increases, too - even if the CO coverage is quickly falling. However, the oxidation of CO proceeds autocatalytic, meaning that surface freed from CO will immediately support water dissociation and enhance the CO oxidation. At the point in time when the CO oxidation rate exceeds that of water dissociation more surface is freed from CO compared to what is lost due to oxide formation, therefore freeing up space for H_2 oxidation. The decreasing overvoltage in turn leads to quick formation of water from surface oxides (the reverse reaction of water dissociation) and enhances the H_2 oxidation rate leading to a further drop in overvoltage. A minimum in overvoltage is reached (maximum in cell voltage) once the H_2 oxidation equilibrium is established on the less CO contaminated catalyst. From this point the cycle repeats itself. The part of the period during which CO is oxidized (when the overvoltage is sufficiently large) will be called "ignition" in the rest of the manuscript. An oscillation-period (interval between red marks in Fig. 2) is thought to start, and to end, at the end of an ignition.

However, compared to the picture of a homogeneous system, where it is believed that the local current density is spatially homogeneous during an oscillation-period, it can be clearly seen in Fig. 2 a-b that the current locally oscillates with the same period as the cell voltage. Connecting the spatio-temporal plot of the current with the explanation of the cycle given above, it can be concluded that the current in the inlet region diminishes after the maximum cell voltage has been reached. This indicates that CO poisoning begins at the inlet of the cell and proceeds downstream. Simultaneously to the current decrease at the inlet, the current in the outlet region increases because of the constant current constraint assured by the load. The result is a current distribution that is flapping with the same period as the cell voltage oscillates.

Finally, note the following two aspects: Firstly, due to the fact that the current distribution of the both channels is almost identical, only one channel will be presented in the rest of the galvanostatic discussion. Secondly, the spatially averaged current density of the two channels oscillates itself (Fig. 2d) and does not coincide with the expected value (predefined by the setup current through the load, the dashed line in Fig. 2d). Likely, this kind of deviation is caused by inhomogeneities in connection with the galvanostatic constraint. Thus, in the CO adsorption phase, a more severe current degradation in one channel is compensated by a less severe current degradation in the other channels (e.g. by the two screened ones, see Fig. 2d). Oppositely,
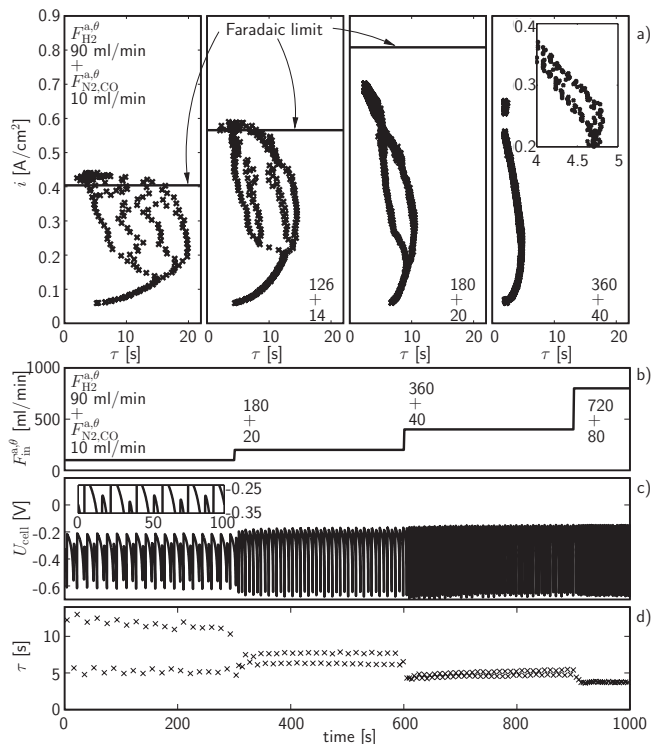
Figure 3. Integral experimental results for galvanostatic H_2, CO electro-oxidation while performing current scans. a) The trajectory of the calculated average current density in the observed cell area (blue line) and the setup value (black line - scan rate of 28 A/3600 s). b) The related trajectory of the cell voltage (blue), the extrema (black boxes) and the temporal average (dash dotted line). c) Polarization curves and d) oscillation periods for different scan rates (red: 28 A/400 s, green: 28 A/1200 s, black: 28 A/3600 s).

Figure 4. Figure a) shows the change of the homogeneous oscillation period during slow current scans for different feed flow rates. b) For a fixed cell current of 0.31 A/cm² steps in the total feed flow rate are carried out. The measured time series of the cell voltage and the related oscillation periods are depicted in c) and d). In all experiments the CO inlet concentrations was 1000 ppm.

in the CO oxidation phase, this altered current distribution is revoked (Fig. 2d). The discrepancy between the setup current density and the measured value in the observed region is even more enhanced at larger currents and can lead to deviations of up to 30% (e.g. Fig. 3a).

Influence of current density and feed flow rate.—In order to search for bifurcation points that were predicted earlier,[9,10] at next the current density is scanned. Of course, the scan rate needs to be sufficiently low in order to avoid transient effects. Therefore, an appropriate current scan rate is validated from integral information before the feed flow rate is varied. Spatially resolved data are taken into account later.

Fig. 3 a-b shows the average current density and the cell voltage in the observed region during a slow scan of the applied current. The current density in the observed region follows the defined value up to a current density of 0.05 A cm⁻² (Fig. 3a). In that interval the cell voltage quickly drops to about −0.35 V (Fig. 3b) due to a lack of free catalyst surface for H_2 oxidation in the course of enhanced CO blockage (e.g. 7). At −0.35 V the behavior changes as the dissociation of H_2O becomes important, allowing the oxidation of CO. However, soon the system loses stability and starts to oscillate (The CO is only oxidized during the ignition phase of the oscillations). As the current scan in Fig. 3 a-b is carried out very slowly, too many oscillations are carried out per current interval to resolve the cell voltage trajectory. Instead, a homogeneously colored blue surface appears. Apart from the time series of the cell voltage itself, the branches that represent the extrema and the temporal average in the oscillatory regime are given in addition to the branch of stable cell voltage at current densities below 0.05 A cm⁻².

The derived polarization curve is shown in Fig. 3c. Additionally, polarization curves for two significantly higher scan rates are depicted. For higher transparency the trajectories of the cell voltage are omitted. From the polarization curves, no differences can be seen except at high current densities, when the current approaches the faradaic limit and H_2 is drawn from the anode outlet tube. In addition to the polarization curves, the periods, τ, of the oscillations are shown in Fig. 3d in the form of a $\tau(i)$ diagram (τ is defined to be the time between subsequent maxima of the cell voltage trajectory). This figure was found to be very sensitive to various cell conditions; thus it is adequate for the comparison of different scan rates. Here, a period doubling bifurcation is found at approximately 0.25 A cm⁻² with a small shift toward positive current density for the largest scan rate (Fig. 3d). This indicates that the two lower scan rates are sufficiently low in order to consider the system as being in a steady (oscillatory) state. However, for subsequent scans the lowest scan rate of 28 A h⁻¹ is chosen in order to obtain a more dense $\tau(i)$ diagram.

The influence of the feed flow rate onto the integral oscillatory behavior is collected in Fig. 4. As can be seen (Fig. 4a), a cascade of period doubling bifurcations is well expressed for small feed flow rates. The bifurcations diminish with increasing feed flow rate until they disappear at about 400 mL min⁻¹. In Fig. 4b the current is held constant while the feed flow rate is increased stepwise. Of course, the trend is the same: The increase of feed flow rate leads to the homogenization of subsequent periods. However, it turns out that the regime with the four fold period does not survive longer than a couple of minutes. Thus the occurrence of this regime in the Fig. 4a (and Fig. 5b) needs to be considered as transient.

Fig. 5 gives an overview of the spatio-temporal results obtained at a constant total feed flow rate of 140 mL min⁻¹. The green crosses in the polarization curve (Fig. 5a) mark the position at which the average profiles of the current distribution are shown in Fig. 5c. These profiles reflect the temporally smoothed current distribution while changing the global current. Looking at these profiles a general trend can be observed: At the lowest current, before the onset of oscillations, the current distribution is rather homogeneous. This indicates that no CO is oxidized and that H_2 oxidation occurs on a homogeneously poisoned surface. At higher currents, the current density increases initially at the outlet. The effect can be rationalized by considering the CO concentration: As CO is oxidized its concentration gradually decreases along the channel and accordingly the coverage of CO is smaller at the outlet. At currents larger than 0.2 A cm⁻² a plateau appears in the outlet region coinciding with a first period doubling bifurcation apparent from Fig. 5b. The high plateau indicates that the CO coverage in the corresponding region is in average rather low and homogeneous. An explanation might be that almost all CO is oxidized in the region upstream and that in the plateau region mainly H_2 is consumed. This idea will be further discussed in the following paragraphs.
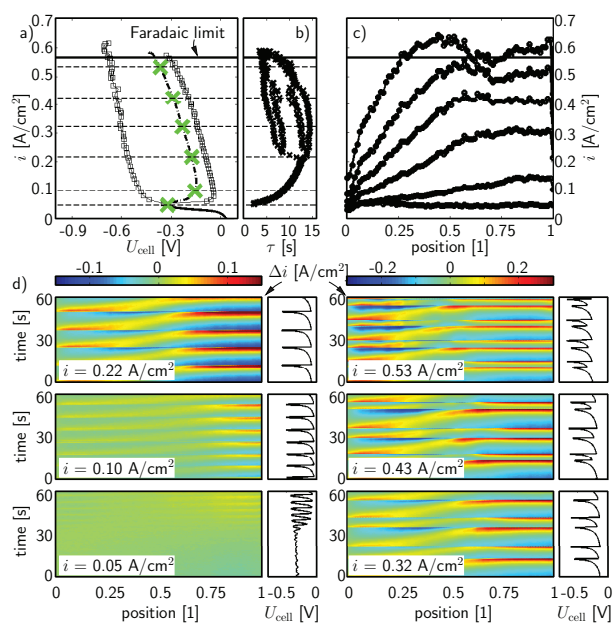
Figure 5. Collected experimental results for a current scan during H_2, CO electro-oxidation: a) Polarization curve. b) Periods. c) Temporally smoothed profiles to see the average trend during the current scan. d) Spatio-temporal plots of the measured spatially distributed current signal (corrected for its temporal space dependent average) starting with the current value given in the plots. The definition of Δi is given in Eq. (9). Scan rate: 28 A/3600 s.

Fig. 5d shows six excerpts of the spatially distributed measurement that were recorded during the scan. But instead of showing the current distribution, only the deviation from the local average $\Delta i(z,t)$ is depicted.

$$\Delta i(z,t) = i(z,t) - \frac{1}{T}\int_0^T i(z,t)\,dt. \qquad [9]$$

Thereby, T is the length of the considered time window (60 s in Fig. 5d). The setup current density at which the excerpts start, is given at the side.

At the lowest current density it can be seen how the system behaves at the onset of the oscillations. While the cell voltage starts to oscillate, the current distribution is rather flat, meaning that the homogeneous state of the system becomes unstable first. With increasing current then also the current distribution starts flapping. At low currents the periods of the oscillations increase with the applied current density (see Fig. 5b). But then, at approximately 0.20 A cm^{-2}, a period doubling bifurcation appears before another period doubling bifurcation is seen at about 0.25 A cm^{-2}. At high currents it is difficult to draw clear conclusions due to the influence of the transport limit. However, it seems that at about 0.4 A cm^{-2} the system starts to behave aperiodic.

When considering the cell voltage in Fig. 5d (0.30 A cm^{-2}) in detail, it is important to note that the short periods always show a more negative minimum, indicating that at the end of a short period more CO is oxidized. Accordingly, after a short period it takes more time until the cell is poisoned to the critical level and the ignition sets in compared to a long period. Taking into account the spatio-temporal plot it can be seen that at the end of each long period (e.g. at $t = 59$ s) the current increase at the outlet is larger compared to the current at the end of a shorter period (e.g. at $t = 46$ s), separating the flapping into a weaker- and a stronger form. This behavior, together with the related cell voltage minimum, shows that during the end of long periods only little CO is present at the outlet leading to a large H_2 oxidation rate. Therefore, the onset of the plateau in the smoothed current profile (Fig. 5c) might indicate the point between an upstream region in which a lot of CO is oxidized during every ignition and a downstream

region in which little CO is oxidized during every second ignition. In the temporal average, then the downstream part of the cell would lead to major H_2 oxidation, while the upstream part is more concerned with CO oxidation. Therefore, the onset of the plateau in the smoothed current profile (Fig. 5c) might indicate the point between an upstream region which is more concerned with CO oxidation and a downstream region of the cell that is preliminary oxidizing H_2.

As mentioned in the introduction, a theoretical prediction for the occurrence of a period doubling bifurcation under decreasing feed flow rate was given in Ref. 9. First of all, in Ref. 9 a criterion was given to refine the feed flow rate at which the influence of the channel CO balance might be expected, namely that the gas residence time in the channel ($T_{res} = L/v$ with L standing for the length of the anodic compartment and v representing the gas velocity) should be larger than the characteristic time of CO adsorption (T_{COad}). In other words: The time for CO transport to the surface shall be affected by the transport along the channel and not be dominated by the transport from the channel to the surface alone. Using the parameters from the experiment shown in Fig. 5, the residence time is found to be 1.6 s. A maximum estimation for T_{COad} can be drawn from oscillations at very large flow rates as CO adsorption in that case mainly determines the length of the period.[1] For a flow rate of 400 mL min-1, a minimal period of 2 s was found (see Fig. 4). Therefore, the conclusion of this argument might be that an influence of the CO channel transport is reasonable. A second agreement between experiment and model regards the qualitative course of the cell voltage. Indeed, the feature of an extended period that follows a more negative cell voltage (anodic overvoltage) during the prior oxidation phase is also well reflected by the model. Discrepancies mainly arise during quantitative comparison.

Influence of the membrane conductivity.—As mentioned in the last section, the membrane resistance is expected to be a reasonable parameter for switching between qualitatively different spatio-temporal behaviors.[10] The regime dominated by strong mean-field coupling (Figs. 3–4) is expected to suddenly change into a spatio-temporal chaotic regime by decreasing the membrane conductivity (increasing the membrane resistance). The purpose of this section is the attempt to experimentally validate this prediction.

The membrane conductivity was changed by varying the cell temperature T_{cell} and the dew point temperature T_{dp}. At each specific pair of temperatures a galvanostatic scan was carried out with a scan rate of 28 A h^{-1}. The scan was interrupted once the cell voltage fell below -1 V. Several values were extracted to characterize the results, these values are: the averaged oscillation period (averaged about the whole scan), the current density at which the oscillations set in and the maximum current density that was obtained in the scan (most likely the cell voltage was minimum then). Furthermore, the highest period doubling bifurcation of the scan was taken in order to see the change of the oscillation behavior: "1T" is for oscillations with one maximum period, "2T" is for oscillations with two maxima period and so forth. Fig. 6 collects the results.

From the information depicted in Fig. 6, three general trends can be derived that have major influence on the results. First, for increasing cell temperature it is found that the oscillation period dramatically decreases. When the dew point temperature is set to 37°C the period drops from 6.1 s at 37°C cell temperature to less than 0.3 s at 60°C cell temperature (The temporal resolution during these scans was about 150 ms. Therefore, 0.3 s represents the technical limit. Likely, the oscillations were faster than this.). This behavior was already observed during the initial finding of the oscillations in PEMFCs[4] and attributed to the change in the CO adsorption.[1] Second, for increasing cell temperature there is a shift of the Hopf point toward larger current densities. It can be explained with an altered CO adsorption/desorption behavior in addition to improved H_2 adsorption.[1] Third, for decreasing rH it was found that the maximum current density that can be driven through the cell, also decreases. For a rH of 75 % the maximal current density is larger than 0.6 A cm^{-2} and decreases to 0.24 A cm^{-2} at 30 % rH. This trend cannot be explained by an increased electrolyte resistance alone and was also present in subsequent experiments (which are not shown) in the absence of CO,
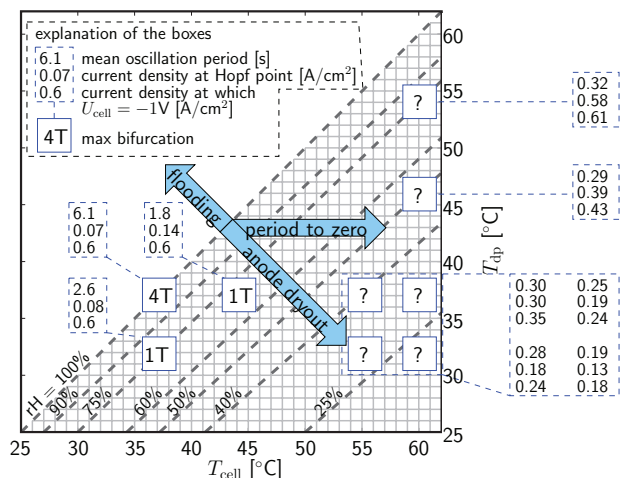
Figure 6. Collected results of galvanostatic scans at various cell- and dew point temperatures. The blue continuous boxes are centered around the pair of temperatures which define the measurement conditions. In the box the highest period doubling bifurcation is written. In the dashed boxes other characteristics of the scans are collected. Additionally, critical influences are indicated that hinder the investigation at high cell temperature (fast oscillations), low conductivity (anode dry out) and high water feed (flooding). Scan rate: 28 A/3600 s.

indicating that this effect has to do with anode dry out. Anode dry out is known to influence conventional PEMFC operation (H_2 supply to anode and O_2 supply to cathode) during operation with poorly humidified gases.[26,27] For co-flow configuration the typical fingerprint is then the following: Close to the inlet the current density as well as the water content in the anode gas is high. Down stream, the anode gas humidity quickly decreases due to the drag of water toward the cathode. Accordingly the current density also diminishes. Oppositely, due to water production at the cathode in conventional PEMFC operation, also the back diffusion enhances such that the anodic rH, as well as the current density, recovers toward the end of the channel once a minimum has been passed. However, as in the present study the current continuously diminishes along the channel it is likely that this is due to the H_2-fed counter electrode used in the present study at which no water production appears.

The final conclusion of studying the influence of the membrane resistance is that no spatio-temporal turbulence, like that predicted in Ref. 10, was found. Arguing about the discrepancy between the experiment and the model, it need to be stated that the model was very simplistic with respect to the water balance. In fact, in the model it was assumed that the gases are saturated at any time and at any place and that the membrane conductivity is also constant in space and time. No water drag and no back diffusion were included because the focus has been on the H_2, CO electro-oxidation. Under these pre-conditions the assumption that the current can be kept stable while the resistance is raised lead to the appearance of spatio-temporal turbulence (if the system dimensions were chosen properly). In the experiment these preconditions fail because of anode dry. In this case the maximum current quickly drops with falling rH and therefore impedes the idea to decrease the current sufficiently in order to find spatio-temporal turbulence. However, as will be shown in the following section, potentiostatic experiments offer an opportunity to search for this regime at high conductivities when anode dry out is absent.

Potentiostatic H_2, CO oxidation.— To show that potentiostatic operation is intrinsically better suited to detect turbulence, the model equations that dominate the system dynamics are initially depicted. At next the individual terms are compared to the previously discussed galvanostatic case. Afterwards, results of potentiostatic H_2, CO electro-oxidation during a voltage scan are presented and the response to voltage steps is depicted. Finally, the impact of the counter electrode is investigated. For that reason the H_2, N_2 mixture (that was up to then

fed into the counter electrode compartment) is replaced by air. In that way the behavior of a conventional PEMFC under the potentiostatic operation with H_2, CO mixtures is illustrated.

Theoretical considerations.—Similar to the model equations for the galvanostatic control[10] also equations for potentiostatic control can be derived (see appendix). The following partial differential equations (Eqs. (10)–(11)) are (in accordance with the galvanostatic model) assumed to dominate the dynamic behavior during H_2, CO electro-oxidation in a PEMFC with straight channel geometry. As during galvanostatic control they describe the evolution of the anodic double layer voltage $\Delta\varphi_a$ and the CO surface coverage θ_{CO}.

$$c_{dl}\frac{\partial \Delta\varphi_a}{\partial t} = -\frac{U + \Delta\varphi_a}{A(R_\Omega + R_{ext})} - f(\Delta\varphi_a, \theta_{CO}) + \frac{d_m^2}{3AR_\Omega L^2}\frac{\partial^2 \Delta\varphi_a}{\partial \zeta^2}$$
$$+ \frac{R_{ext}\left(\overline{\Delta\varphi_a} - \Delta\varphi_a\right)}{AR_\Omega(R_\Omega + R_{ext})}, \qquad [10]$$

$$\gamma C_t^* \frac{\partial \theta_{CO}}{\partial t} = g(\Delta\varphi_a, \theta_{CO}). \qquad [11]$$

In the Eqs. (10)–(11) the homogeneous system is again inherent at each reaction site

$$c_{dl}\frac{d\Delta\varphi_a}{dt} = -\frac{U + \Delta\varphi_a}{A(R_\Omega + R_{ext})} - f(\Delta\varphi_a, \theta_{CO}), \qquad [12]$$

$$\gamma C_t^* \frac{d\theta_{CO}}{dt} = g(\Delta\varphi_a, \theta_{CO}). \qquad [13]$$

Other terms in Eq. (10) are the (locally acting) migration coupling term and the (globally acting) mean-field coupling term. The new variable R_{ext} stands for an external resistance (lines etc., see Fig. 1 c-d). It influences, in contrast to Eq. (3), mean-field coupling as well as the local system.

Galvanostatic control (Eq. (3)) can be re-obtained from Eq. (10) if $I_{load} = -U/R_{ext}$ is kept constant while increasing the external resistance to infinite values ($R_{ext} \to \infty$). In that case the factor controlling the mean-field coupling term becomes maximal (for a fixed R_Ω). Oppositely, the influence of the global coupling term vanishes for decreasing external resistance and disappears for $R_{ext} \to 0$. Therefore, the control of R_{ext} during potentiostatic operation allows to diminish mean-field coupling alone. It leaves migration coupling unchanged. This is in contrast to the change of R_Ω during galvanostatic control, where both coupling terms where affected.

As in the model prediction of the galvanostatic section a dominant migration coupling term lead to spatio-temporal turbulence,[10] it is reasonable to assume that spatio-temporal turbulence might be found with potentiostatic control more easily compared to galvanostatic control. The only necessary precondition is that the homogeneous potentiostatic system can also oscillate at lower R_{ext}.

Scanning the cell voltage.—Fig. 7 collects the integral signals and the spatio-temporal plots for a voltage scan with a scan rate of 1 V/2000 s. In Fig. 7a the typical polarization curve can be seen. The branch at high cell voltages (beyond −0.35 V) is characterized by a very little slope, while the branch at lower cell voltage (beneath −0.35 V) shows a very steep decrease. The slope of this last branch can be explained almost entirely with the membrane losses. Accordingly, the change in the (spatially averaged) anodic double layer voltage is minor. Current density profiles at specific cell voltages (indicated in Fig. 7a with colored crosses) are depicted in Fig. 7b. In comparison with Fig. 5c here the profiles are not smoothed but represent the true current distribution at a specific point in time. In general an increase in current profile toward the outlet of the cell can be seen. This trend is pronounced the lower the cell voltage is and starts at the voltage when CO can be oxidized (−0.35 V). Therefore, it seems that this effect relates to the diminishing CO mole fraction due to cumulative CO oxidation. However, in a certain voltage interval the profiles show spikes (e.g. red curve in Fig. 7b) while the integral polarization curve (Fig. 7a) seems to be smooth. The meaning of these spikes becomes
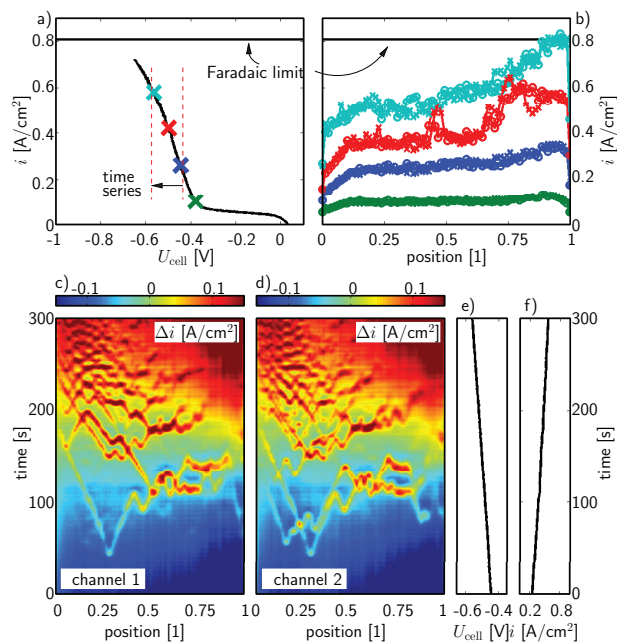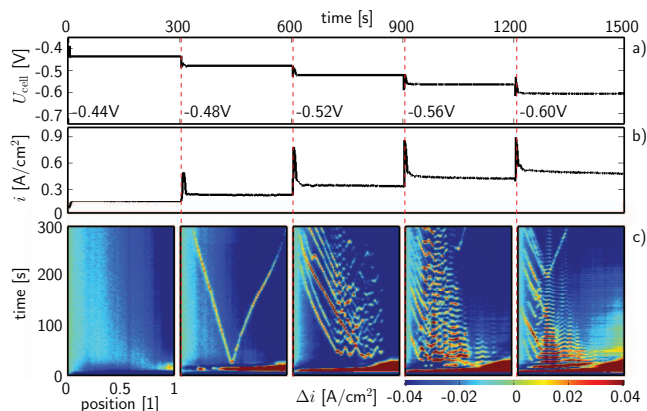
Figure 7. Collected experimental results for a voltage scan during potentiostatic H_2, CO electro-oxidation: a) Polarization curve. b) Current density profiles at specific moments during the scan. × and ○ represent the individual channels. c-d) Spatio-temporal plots of the measured spatially distributed current signal (corrected for its temporal space dependent average) for both channels. e-f) Cell voltage and average current density in the observed region. Scan rate: 1 V/2000 s.

obvious in the Figs. 7 c-d which show the current density deviations from the local average in the time interval depicted in Fig. 7a.

Globally, the spatio-temporal plots turn from blue at high cell voltages (−0.44 V) to red at low cell voltages (−0.58 V) due to the increasing current density. However, apart from that, several straight lines can be seen which depict the propagation of pulses. Apparently, below a certain cell voltage (−0.46 V in the present configuration) current bumps form at arbitrary positions that soon split into two pulses that travel in the down- and upstream direction. Thereby, the pulses seem to be very local objects as they do not appear necessarily in both channels simultaneously (e.g. compare Fig. 7 c with d at 50 s). As the traveling speed is independent from the direction (about 1.7 cm/min) and much slower than the gas velocity (about 90 cm/min) they likely represent objects restricted to the active area. Another interesting observation is that some of the pulses extinguish each other (Fig. 7c at 120 s at the position 0.4) while in other situations they seem to cross without noticing (Fig. 7c at 160 s at the position 0.4). However, it is difficult to conclude that these pulses truly cross. It could also be that the pulse in-plane extension is much smaller than the individual segments of the measurement board. In that case it would seem that they cross while they pass each other closely. Crossing pulses would indicate that the present understanding of H_2, CO electro-oxidation is incomplete, for the following reason: After the pulse has crossed a certain place, the CO coverage is lower at that place and this site is necessarily not excitable until a sufficient CO surface coverage has recovered. Therefore, left and right of the position where two pulses intersect the surface would not be excitable, neither.

Stepping the cell voltage.—Fig. 8 collects the integral signals and the spatio-temporal plots of one of the two channels after stepping through the voltage. After each of the steps, a characteristic overshoot in the current can be seen (Fig. 7b). The related irregularities in the cell voltage (Fig. 7a) are a consequence of the control loop of the load. The overshoot indicates the presence of CO oxidation (more effective at the outlet: see Fig. 7c) and is absent at cell voltages that are larger than −0.4 V. Late after the residence time (about 1.5 s) has passed, the

Figure 8. Collected experimental results for sudden steps of the voltage during potentiostatic H_2, CO electro-oxidation. a) The defined cell voltage profile. b) The related average current density in the observed region. c) Spatio-temporal plots of the measured spatially distributed current signal (corrected for its temporal space dependent average) for one of the two channels beginning at the voltage step.

overshoot disappears (more than 20 s), indicating that after a rather effective ignition, triggered by the step, it takes some time to supply sufficient CO to passivate the surface again.

Apart from this general feature also other phenomena can be identified. First of all, the second step in Fig. 7a to −0.48 V triggers two pulses that are formed by the splitting of a single perturbation at the center of the channel (Fig. 7c). While the pulse that moves upstream travels with constant speed, the pulse that travels downstream undergoes some velocity variation. The reason for this alteration is unclear and also no general feature.

After the next step to −0.52 V, in the center of the channel some oscillations are found to die out in the course of minutes. The spatial variation in this central part is rather unordered. Evidently, these small oscillations trigger a bunch of pulses that travel upstream. Some of these pulses travel a little faster than others and again it seems that some cross each other without interaction. However, as discussed above it might be caused by the finite spatial resolution of the measurement device. It is likely that the pulses only pass each other closely.

At lower cell voltage two general observations can be made. The one is, that after the step a part of the channel starts to oscillate homogeneously (with a stricter phase relation between adjacent sites than after the steps before). But also these structures are unstable and crumble as time passes. The other trend is that the region of the channel, in which some structure appears, shifts upstream, leaving at low cell voltages a major downstream part of the cell non-oscillatory. It is unlikely that in this region absolutely no CO is present on the surface, but it seems that the local concentration is low enough to stabilize the downstream part.

The Influence of the counter electrode.—Finally, the influence of a counter electrode should be depicted with the help of two experiments. Compared to the potentiostatic experiments presented above, air is fed into the counter electrode compartment while the anode configuration is left unchanged. The first experiment is a voltage scan and the results are collected in Fig. 9. The second experiment is a single step of the cell voltage and the results are shown in Fig. 10.

The polarization curve during the scan (Fig. 9) starts at an open circuit potential of 0.9 V. For decreasing cell voltage the current initially increases very slowly before the much steeper slope indicates the onset of CO oxidation. This general course is, apart from the shift along the cell voltage axis, identical to the behavior found with the H_2-fed counter electrode (Fig. 7). However, at about 0.2 V a maximum current is reached at which rather strong fluctuations of the current are observed. In other experiment the onset of these oscillations appeared before the maximum was reached. It can therefore not be attributed to this specific feature. The low maximum current
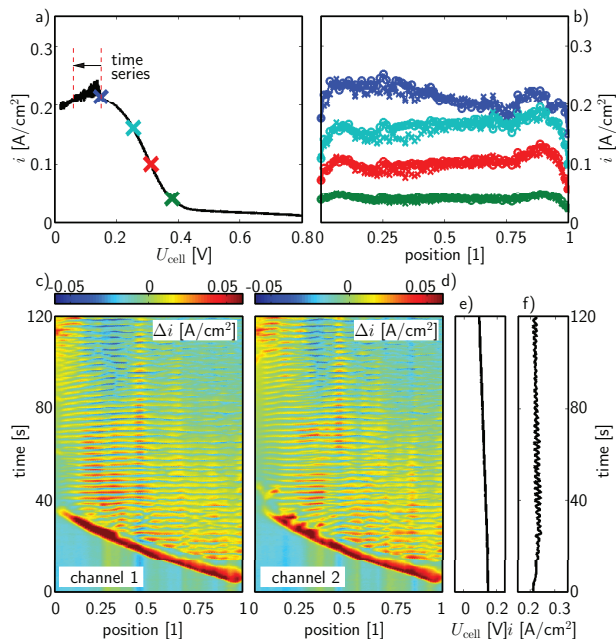
Figure 9. Collected experimental results for a voltage scan during potentiostatic H_2, CO electro-oxidation with an air-fed counter electrode. a) Polarization curve. b) Current density profiles at specific moments during the scan. $\times$ and $\circ$ represent the individual channels. c-d) Spatio-temporal plots of the measured spatially distributed current signal (corrected for its temporal space dependent average) for both channels. e-f) Cell voltage and average current density in the observed region. Scan rate: 1 V/2000 s.

density of $0.2\,A\,cm^{-2}$ in comparison with the high current densities obtained for the H_2-fed counter electrode (Fig. 5a) indicates the appearance of ongoing flooding. While the differences in the separate channel profiles at 0.30 V (red curves) and 0.24 V (cyan curves) given in Fig. 9b can be explained with minor flooding, the initial decrease of current along the profiles at lowest cell voltage (0.16 V blue curves) is likely to be caused by more severe flooding. However, the subsequent current increase at the position 0.75 (in the blue curve) marks a front of an upstream traveling pulse.

The related spatio-temporal patterns are presented in the Figs. 9c-d. The sequence starts at the time when the cell voltage is 0.15 V. Clearly, a pulse that starts at the outlet of the cell quickly travels upstream. The speed of this pulse is much faster than in the sce-
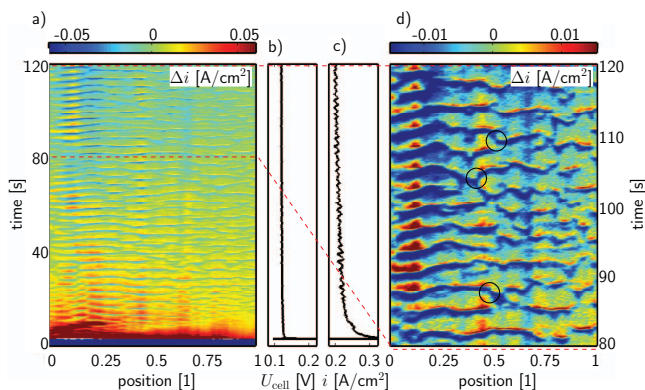
Figure 10. a) Spatio-temporal plots of the measured spatially distributed current signal (corrected for its temporal space dependent average) of one arbitrary channel after a step into the voltage regime at which CO can be oxidized. b) The cell voltage. c) The average current density in the observed two-channel-region. d) Magnified spatio-temporal plot of the last 40 s. In this experiment, the cathode was fed with air.

narios with the H_2-fed cathode (here: $30\,cm\,min^{-1}$). Once it crossed, the sites are not excitable for a short time ($3-4\,s$). In that time no fluctuations appear at the position where the pulse has just passed. After the delay some oscillations appear and adjacent sites synchronize. However, the in phase-regions (the connected red regions in Figs. 9 c-d) bend weakly, indicating phase turbulence. At other sites (e.g. Fig. 9c at $x = 0.4$ and $t = 35\,s$) discontinuities can be observed, indicating defect turbulence. Also note the difference between the both channels, indicating phase changes also in the direction perpendicular to the gas flow. Both scenarios, phase- and defect turbulence, are typical for a Benjamin-Feir instability[28–30] in which a plane wave becomes unstable due to phase repulsion of adjacent oscillators. Although the Benjamin-Feir instability has experienced some numerical investigation,[29,31,32] experimental evidence is seldom yet. The only experimental result (to our knowledge) depicting phase and defect turbulence in electrochemical systems was reported on the oscillatory H_2 electro-oxidation in acidic electrolyte with a Pt ring.[33,34]

Finally, a simple step from ocv into the oscillatory regime (U_{cell} = 0.12 V) was carried out. The corresponding spatio-temporal plot of one of the channels is given in Fig. 10, together with an excerpt that presents the behavior in larger detail at the end of the time series. Again, phase- and defect turbulence is found. Some of the defects are encircled.

In comparison to the potentiostatic experiments with the H_2-fed counter electrode the discrepancies in the patterns can be speculated to mainly originate from two differences: Firstly, due to water production in case of the air-fed counter electrode the resistance of the membrane alters for changing current because in that case it can only be controlled poorly with the feed flow water content. Secondly, the more expressed oscillations in case of the air-fed cathode might relate to the larger cathode overvoltage as the electrode is more lossy compared to the cathode at which H_2 evolution occurs. In the following these candidates should be inspected in more detail.

Regarding the lower membrane resistance in case of water production at the cathode, it can be seen from Eq. (10) that the influence of both coupling terms is enhanced. However, in Fig. 8 it seems that the outlet region of the cell is not only not oscillatory instable but even not excitable as no pulses travel in that direction. This fact indicates that it is not the coupling terms but the dynamics of the homogeneous system (Eqs. (12)–(13)) which inhibit the oscillations in the downstream part. Indeed, the membrane resistance has impact on the homogeneous system, too (Eq. (12)). For a homogeneous HN-NDR system a decreasing Ohmic resistance (steeper load line - see Ref. 21 and below) would in fact drive the system toward extinction of the oscillations, oppositely to what is seen above. However, the influence of changing membrane resistance should be very little as during the experiments with the air-fed cathode the membrane applied was as double as thick as in the case with the H_2-fed cathode. In fact, a 1 kHz-impedance of about $7 \pm 2\,m\Omega$ for the first and $9 \pm 2\,m\Omega$ for the later experiment were measured.

Considering the impact of the cathode overvoltage with the help of Eq. A14, the overvoltages $\eta_{a/c}$ ($\eta_{a/c} = \Delta\varphi_{a/c} - \Delta\varphi_{a/c}^0$) of the homogeneous system are given by (see appendix for derivation)

$$C_{dl,a}\frac{d\eta_a}{dt} = \frac{(\Delta\varphi_c^0 - \Delta\varphi_a^0 - U) - \eta_a + \eta_c}{A(R_\Omega + R_{ext})} - f\left(\eta_a + \Delta\varphi_a^0, \theta_{CO}\right),$$

$$[14]$$

$$-C_{dl,c}\frac{d\eta_c}{dt} = \frac{(\Delta\varphi_c^0 - \Delta\varphi_a^0 - U) - \eta_a + \eta_c}{A(R_\Omega + R_{ext})} - i_{reac,c}(\eta_c).\ [15]$$

with $\Delta\varphi_{a/c}^0$ standing for the anodic/cathodic equilibrium double layer voltages. The term $(\Delta\varphi_c^0 - \Delta\varphi_a^0 - U)$ represents the difference between open circuit cell voltage and actual cell voltage. For both applied cathodes it is always positive and increases with decreasing voltage U. The whole first term at the right hand side of Eq. (14) is known as "load line" from conventional electrochemistry. It yields the

current, passing through the load, as a function of the working electrodes overvoltage. The new aspect of the load line above, is that in conventional electrochemical system no influence of η_c can be found due to the application of reference electrodes. However, using an explicit expression for $i_{reac,c}$, Eq. (15) would yield an equation of the form $\eta_c(\eta_a)$ that could be entered into Eq. (14) to obtain an anodic load line similar to the conventional type (dependent only on η_a). The load line is such an interesting object, because its slope determines (for a given $i_{reac,a}$) if the HN-NDR system can oscillate or not. For an HN-NDR system it is true that, the steeper the load line is (the smaller $R_\Omega + R_{ext}$ is), the smaller is the voltage interval in which oscillations occur. At some critical slope the oscillations will extinct. Assuming the most simple rate approach for the faradaic cathodic current $i_{reac,c} = -k\eta_c$, with k representing some positive constant, it follows from the steady state condition applied to Eq. (15) that

$$\eta_c = a\eta_a - b, \qquad [16]$$

with a and b being some positive constants that vanish for infinite k. Entering this expression into Eq. (14) it becomes apparent that the slope of the load line is flattened. So, a lossy counter electrode ($k < \infty$) acts in this respect like an additional series resistance, supporting oscillations in the HN-NDR system.

Conclusions

In the present contribution H_2, CO electro-oxidation in a PEMFC with a H_2-fed counter electrode was investigated at $37°C$ with the help of a printed circuit board for distributed current measurement. The cell design was motivated by the mathematical model developed in Ref. 9 and consists of six parallel channels of 14.4 cm length.

The experiments at galvanostatic control, presented in the first part of the discussion, clearly verified the predictions for the mean-field coupled regime proposed in Refs. 9 and 10: At high humidification and high feed flow rate the current is flapping and one minimum per period appears in the cell voltage in the whole oscillatory current range. If the feed flow rate is decreased, a period doubling bifurcation appeared at a certain critical current. However, the oscillation periods as well as the specific positions of the bifurcations (Hopf- and period doubling bifurcation) vary between model and experiment. On the one hand the reason might be that there is a certain mismatch between parameters chosen for the earlier model study and parameters applied in the experiment (catalyst loading, temperatures, etc.). But on the other hand, there is also some uncertainty in the kinetic parameters of the model. Therefore, a quantitative model description requires additional adaptation work.

The presence of spatio-temporal turbulence during galvanostatic control could not be verified due to anodic dry out. Therefore, experiments under potentiostatic control were taken into account. The potentiostatic experiments, carried out with a H_2-fed cathode, demonstrated the occurrence of pulses, a phenomenon which was not studied by means of modeling for this system yet. Furthermore, unstable oscillations were found after sudden voltage steps into the CO oxidation regime. Potentiostatic experiments with an air-fed cathode revealed less pulses but well expressed phase- and defect turbulence.

Discussing the deeper impact of the air fed cathode, it was argued that this more lossy counter electrode might act as an additional resistor, supporting oscillations in this HN-NDR system. Further studies with varying oxygen concentrations might help to clearify this conjecture.

Appendix

The purpose of this section is to derive specific PDEs for the double layer evolution. The related improvement in transparency leads to an altered understanding of a fuel cell, namely as being composed of local dynamical systems that interact via migration currents and the global control implied by the external circuit (including the load constraint).

Fig. 11 sketches the idealized PEMFC under consideration, consisting of an electrolyte with double layers and an embedding electrical control circuit. During the following derivation these three preconditions need to hold: 1) The system can be considered as two-dimensional (the direction perpendicular to the gas flow direction is assumed to be homogeneous). 2) The conductivity of the membrane is constant in time and space. 3) The dimension of the electrolyte is such that $d_m \ll L$.

The derivation starts by solving the potential field in the electrolyte and proceeds via the approximation of the current that passes from the electrolyte into the double layer. Afterwards an equation for the electric control circuit is solved explicitly and entered into the double layer equations to obtain the general result. At the very end some limiting cases are considered to link the derived formulas to the equations used earlier in this manuscript.

The distribution of the electric field in a homogeneous (2-dimensional) electrolyte is given by the following Laplace equation and appropriate boundary conditions

$$\frac{\partial^2 \varphi}{\partial y^2} + \frac{\partial^2 \varphi}{\partial z^2} = 0 \quad \text{(Laplace equation)}, \qquad [A1]$$

$$\frac{\partial \varphi}{\partial z}\Big|_{z=0} = \frac{\partial \varphi}{\partial z}\Big|_{z=L} = 0 \quad \text{(left and right boundary condition)}, \qquad [A2]$$

$$\varphi|_{y=0} = \phi(z,t) \quad \text{(boundary condition at top)}, \qquad [A3]$$

$$\varphi|_{y=d_m} = \psi(z,t) \quad \text{(boundary condition at bottom)}. \qquad [A4]$$

This equation can be solved with the help of a separation approach followed by a Fourier series approach for the two remaining ODEs. Incorporating then the boundary conditions (Eqs. (A2)–(A4)) one finds the following solution for the potential field in the electrolyte $\varphi(y,z,t)$

$$\varphi(y,z,t) = \phi^0 - (\phi^0 - \psi^0)\frac{y}{d_m} + 2\sum_{n=1}^{\infty} \cos\left(\frac{n\pi z}{L}\right)$$
$$\times \left(\phi^n A_n + \psi^n \cosh\left(\frac{n\pi d_m}{L}\right)(B_n - A_n)\right), \qquad [A5]$$

with A_n and B_n being the functions

$$A_n(y) = \frac{\sinh\left(\frac{n\pi}{L}(d_m - y)\right)}{\sinh\left(\frac{n\pi d_m}{L}\right)} \quad \text{and} \quad B_n(y) = \frac{\cosh\left(\frac{n\pi}{L}(d_m - y)\right)}{\cosh\left(\frac{n\pi d_m}{L}\right)}. \qquad [A6]$$

The set of variables ϕ^n and ψ^n represent the real Fourier transforms at frequency $\frac{n\pi d_m}{L}$ of the related boundary condition
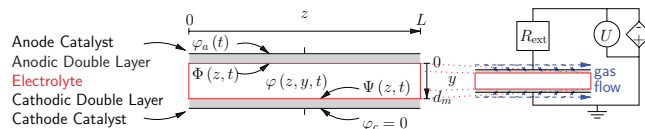
$$\phi^n(t) = \frac{1}{L}\int_0^L \phi \cos\left(\frac{n\pi z}{L}\right)dz \quad \text{and} \quad \psi^n(t) = \frac{1}{L}\int_0^L \psi \cos\left(\frac{n\pi z}{L}\right)dz. \qquad [A7]$$

Generally, the equation for the evolution of the anodic double layer voltage $\Delta\varphi_a$ is given by

$$c_{dl,a}\frac{\partial \Delta\varphi_a}{\partial t} = -\kappa \frac{\partial \varphi}{\partial y}\Big|_{y=0} - i_{reac,a}. \qquad [A8]$$

Thereby, the parameters $c_{dl,a}$ and κ represent the electric double layer capacity and the membrane conductivity. The function $i_{reac,a}$ is a placeholder for currents resulting from electrochemical reactions. For the consideration in this appendix this function is not of interest. The second term in Eq. (A8) can be evaluated with the help of the explicit expression for the potential field in the electrolyte (Eq. (A5)). If the appearing hyperbolic functions are developed for small d_m/L in form of a Laurent series (until second order), then it is found that

$$-\kappa \frac{\partial \varphi}{\partial y}\Big|_{y=0} = -\kappa\left(\frac{\psi - \phi}{d_m} + \frac{d_m}{3}\frac{\partial^2 \phi}{\partial z^2} + \frac{d_m}{6}\frac{\partial^2 \psi}{\partial z^2}\right). \qquad [A9]$$

Figure 11. The electric setup of the considered "one dimensional" PEMFC system together with the used abbreviations. Note, that for an infinite external resistance ($R_{ext} \to \infty$) the operation mode switches from potentiostatic to galvanostatic control when the ratio $I_{load} = U/R_{ext}$ is held constant.

With the definition of the double layer voltages and the choice of an arbitrary "zero" potential at the counter electrode current collector

$$\Delta\varphi_a = \varphi_a - \phi, \tag{A10}$$

$$\Delta\varphi_c = \varphi_c - \psi = -\psi, \tag{A11}$$

Eq. (A9) becomes

$$-\kappa\frac{\partial\varphi}{\partial y}|_{y=0} = -\kappa\left(\frac{\Delta\varphi_a - \Delta\varphi_c}{d_m} - \frac{\varphi_a}{d_m} + \frac{d_m}{3}\frac{\partial^2\Delta\varphi_a}{\partial z^2} + \frac{d_m}{6}\frac{\partial^2\Delta\varphi_c}{\partial z^2}\right). \tag{A12}$$

Up to that point the potential field between the anodic and the cathodic current collector is described. The final equation need to characterize the embedding of the cell into the external circuit. It needs to yield φ_a (the potential of the anodic current collector) and is derived from Kirchhoffs loop law of the overall circuit (Fig. 11).

$$\varphi_a = -U - R_{ext}I, \tag{A13}$$

in which U stands for the potential difference measured by the load. The total current I can be found by integrating Eq. (A12) along the channel coordinate z. If the result is entered into Eq. (A12), one finally obtains the desired equation for the evolution of the anodic double layer potential from Eq. (A8), in which the influence of the electrolyte is now included.

$$c_{dl,a}\frac{\partial\Delta\varphi_a}{\partial t} = -\frac{U + \Delta\varphi_a - \Delta\varphi_c}{A(R_\Omega + R_{ext})} - i_{reac,a} + \frac{d_m^2}{6AR_\Omega L^2}\left(2\frac{\partial^2\Delta\varphi_a}{\partial\zeta^2} + \frac{\partial^2\Delta\varphi_c}{\partial\zeta^2}\right)$$
$$+ \frac{R_{ext}\left(\overline{\Delta\varphi_a} - \overline{\Delta\varphi_c} - \Delta\varphi_a + \Delta\varphi_c\right)}{AR_\Omega(R_\Omega + R_{ext})}. \tag{A14}$$

In this expression the membrane conductivity κ was avoided in favor of the membrane resistance $R_\Omega = \frac{d_m}{\kappa A}$. Similarly, the channel coordinate z was replaced by the dimensionless variable ζ ($\zeta = \frac{z}{L}$). The expressions $\overline{\Delta\varphi_{a/c}}$ stand for the spatially averaged values of the respective double layer voltages. At the left and right boundary "no-flux" conditions enable. Of course, the same procedure can be carried out also for the cathode double layer. The result is then

$$-c_{dl,c}\frac{\partial\Delta\varphi_c}{\partial t} = -\frac{U + \Delta\varphi_a - \Delta\varphi_c}{A(R_\Omega + R_{ext})} - i_{reac,c} +$$
$$\frac{d_m^2}{6AR_\Omega L^2}\left(\frac{\partial^2\Delta\varphi_a}{\partial\zeta^2} + 2\frac{\partial^2\Delta\varphi_c}{\partial\zeta^2}\right) + \frac{R_{ext}\left(\overline{\Delta\varphi_a} - \overline{\Delta\varphi_c} - \Delta\varphi_a + \Delta\varphi_c\right)}{AR_\Omega(R_\Omega + R_{ext})}. \tag{A15}$$

In this equation the parameters $c_{dl,c}$ and $i_{reac,c}$ stand for the electric double layer capacity and the faradaic currents at the cathode. Please note the high symmetry between the last two equations (Eqs. (A14)–(A15)): Apart from the faradaic reactions the only changes appear in the factor controlling the diffusion-like migration coupling term.

Finally, some limits of the set of equations (A14) and (A15) shall be considered: In case that the counter electrode is negligible ($\Delta\varphi_c \approx 0$) Eq. (A14) becomes

$$c_{dl,a}\frac{\partial\Delta\varphi_a}{\partial t} = -\frac{U + \Delta\varphi_a}{A(R_\Omega + R_{ext})} - i_{reac,a} + \frac{d_m^2}{3AR_\Omega L^2}\frac{\partial^2\Delta\varphi_a}{\partial\zeta^2} + \frac{R_{ext}\left(\overline{\Delta\varphi_a} - \Delta\varphi_a\right)}{AR_\Omega(R_\Omega + R_{ext})}, \tag{A16}$$

which is the formulation used during the theoretical considerations of the potentiostatic control with the H_2-fed cathode. For the galvanostatic limit $R_{ext} \to \infty$, while keeping $-U/R_{ext} = I$ constant, the equation used in the section "Mechanistic Details and Predictions" is obtained

$$c_{dl,a}\frac{\partial\Delta\varphi_a}{\partial t} = \frac{I}{A} - i_{reac,a} + \frac{d_m^2}{3AR_\Omega L^2}\frac{\partial^2\Delta\varphi_a}{\partial\zeta^2} + \frac{1}{AR_\Omega}\left(\overline{\Delta\varphi_a} - \Delta\varphi_a\right). \tag{A17}$$

In case that no gradients appear (the functions $i_{reac,a/c}$ do not depend on ζ and $\frac{\partial^2\Delta\varphi_{a/c}}{\partial\zeta^2} \to 0$) the system reduces to the homogeneous form. With the introduction of overvoltages

$$\eta_{a/c} = \Delta\varphi_{a/c} - \Delta\varphi_{a/c}^0, \tag{A18}$$

with $\Delta\varphi_{a/c}^0$ standing for the equilibrium double layer voltages, the result reads

$$c_{dl,a}\frac{d\eta_a}{dt} = \frac{(\Delta\varphi_c^0 - \Delta\varphi_a^0 - U) - \eta_a + \eta_c}{A(R_\Omega + R_{ext})} - i_{reac,a}, \tag{A19}$$

$$-c_{dl,c}\frac{d\eta_c}{dt} = \frac{(\Delta\varphi_c^0 - \Delta\varphi_a^0 - U) - \eta_a + \eta_c}{A(R_\Omega + R_{ext})} - i_{reac,c}, \tag{A20}$$

which is the formulation used during the discussion of the potentiostatic control with the air-fed cathode.

References

1. T. Kadyk, S. Kirsch, R. Hanke-Rauschenbach, and K. Sundmacher, *Electrochimica Acta*, **56**, 10593 (2011).
2. W. Gu, D. R. Baker, Y. Liu, and H. A. Gasteiger, in *Handbook of Fuel Cells*, Vol. 6, Wiley, New York (2009).
3. P. P. Lopes, E. A. Ticianelli, and K. S. Freitas, *Electrocatal.*, **1**, 200 (2010).
4. J. X. Zhang and R. Datta, *J. Electrochem. Soc.*, **149**, A1423 (2002).
5. J. X. Zhang and R. Datta, *Electrochem. Solid-State Lett.*, **7**, A37 (2004).
6. R. Hanke-Rauschenbach, C. Weinzierl, M. Krasnik, L. Rihko-Struckmann, H. Lu, and K. Sundmacher, *J. Electrochem. Soc.*, **156**, B1267 (2009).
7. P. P. Lopes, E. A. Ticianelli, and H. Varela, *J. Power Sources*, **196**, 84 (2011).
8. R. Hanke-Rauschenbach, M. Mangold, and K. Sundmacher, *Rev. Chem. Eng.*, **27**, 23 (2011).
9. R. Hanke-Rauschenbach, S. Kirsch, R. Kelling, C. Weinzierl, and K. Sundmacher, *J. Electrochem. Soc.*, **157**, B1521 (2010).
10. S. Kirsch, R. Hanke-Rauschenbach, and K. Sundmacher, *J. Electrochem. Soc.*, **158**, B44 (2011).
11. R. Hanke-Rauschenbach, S. Kirsch, and K. Sundmacher, in *Computer Aided Process Engineering*, Vol. 29, Elsevier, Amsterdam (2011).
12. M. Schulze, E. Gulzow, S. Schonbauer, T. Knori, and R. Reissner, *J. Power Sources*, **173**, 19 (1997).
13. L. C. Perez, L. Brandao, L. M. Sousa, and A. Mendes, *Renewable Sustainable Energy Rev.*, **15**, 169 (2011).
14. S. J. C. Cleghorn, C. R. Derouin, M. S. Wilson, and S. Gottesfeld, *J. Appl. Electrochem.*, **28**, 663 (1998).
15. D. J. L. Brett, S. Atkins, N. P. Brandon, and V. Vesovic, *Electrochem. Comm.*, **3**, 628 (2001).
16. J. Stumper, S. A. Campbell, D. P. Wilkinson, and M. C. Johnson, *Electrochimica Acta*, **43**, 3773 (1998).
17. Z. Liu, Z. Mao, B. Wu, L. Wang, and V. M. Schmidt, *J. Power Sources*, **141**, 205 (2005).
18. Ch. Wieser, A. Helmbold, and E. Glzow, *J. Appl. Electrochem.*, **30**, 803 (2004).
19. A. B. Geiger, R. Eckl, A. Wokaun, and G. G. Scherer, *J. Electrochem. Soc.*, **151**, A394 (2004).
20. J. X. Zhang, J. D. Fehribach, and R. Datta, *J. Electrochem. Soc.*, **151**, A689 (2004).
21. K. Krischer, in *Advances in Electrochemical Science and Engineering*, Vol. 8, Wiley-VCH, Weinheim (2003).
22. S. Kirsch, R. Hanke-Rauschenbach, A. El-Sibai, D. Flockerzi, K. Krischer, and K. Sundmacher, *J. Phys. Chem. C*, **115**, 25315 (2011).
23. A. Mota, P. P. Lopes, E. A. Ticianelli, E. R. Gonzalez, and H. Varela, *J. Electrochem. Soc.*, **157**, B1301 (2010).
24. H. A. Gasteiger, N. M. Markovic, and P. N. Ross, *J. Phys. Chem.*, **99**, 8290 (1995).
25. Y. Sone, P. Ekdunge, and S. Simonsson, *J. Electrochem. Soc.*, **4**, 1254 (1996).
26. Q. Dong, M. M. Mench, S. Cleghorn, and U. Beuscher, *J. Electrochem. Soc.*, **152**, A2114 (2005).
27. Y. Wang and C. Y. Wang, *Electrochimica Acta*, **51**, 3924 (2006).
28. T. B. Benjamin and J. E. Feir, *J. Fluid Mech.*, **27**, 417 (1967).
29. B. I. Shraiman, A. Pumir, W. VanSaarlos, P. C. Hohenberg, H. Chate, and M. Holen, *Physica D*, **57**, 241 (1992).
30. A. Pikovsky, M. Rosenblum, and J. Kurths, *Synchronization*, Cambridge University Press, Cambridge/UK (2001).
31. J. T. Stuart and R. C. Diprima, *Proc. R. Soc. Lond. A*, **362**, 27 (1978).
32. H. Segur, D. Henderson, J. Carter, J. Hammack, C. M. Li, D. Pheiff, and K. Socha, *J. Fluid Mech.*, **539**, 229 (2005).
33. H. Varela, C. Beta, A. Bonnefont, and K. Krischer, *Phys. Rev. Lett.*, **94**, 174104 (2005).
34. H. Varela, C. Beta, A. Bonnefont, and K. Krischer, *Phys. Chem. Chem. Phys.*, **7**, 2429 (2005).